
Article:
Pessu, F orcid.org/0000-0003-3587-4309, Barker, R orcid.org/0000-0002-5106-6929 and Neville, A orcid.org/0000-0002-6479-1871 (2016) Understanding Pitting Corrosion Behavior of X65 Carbon Steel in CO2-Saturated Environments: The Temperature Effect. Corrosion, 72 (1). pp. 78-94. ISSN 0010-9312

https://doi.org/10.5006/1338

Understanding Pitting Corrosion Behavior of X-65 Carbon Steel in CO_2-Saturated Environments: The Temperature Effect

Frederick Pessu, Richard Barker and Anne Neville

Institute of Functional Surfaces (iFS)

School of Mechanical Engineering, University of Leeds

Leeds, LS2 9JT, UK

ABSTRACT

A systematic study examining the pitting corrosion behavior of X-65 carbon steel in CO_2-saturated 10 wt. % NaCl brine is presented. The paper examines the impact of changes in a key environmental parameter (temperature) on the pitting corrosion processes of carbon steel. Pit propagation studies are conducted in static conditions at different operational temperatures. The evolution of corrosion products on carbon steel is followed over 168 hours of immersion and their characteristics are related to initiation and growth of pits on the steel surface. The developed corrosion products are studied through the use of X-ray diffraction and scanning electron microscopy. The extent of pitting is evaluated through the implementation of surface interferometry to study discrete pit geometry; namely, the size and depth, whilst the general corrosion rate is evaluated using linear polarization resistance measurements. The results indicate that pitting corrosion dominates the general thickness loss of the material in conditions where the morphology of the corrosion product layer is predominantly cementite (Fe_3C) and/or a form of iron carbonate ($FeCO_3$) often referred to in literature as 'amorphous' $FeCO_3$. At 30^{o}C and 50^{o}C, pit propagation continued unhindered despite the growth of an amorphous $FeCO_3$ layer. However, at 80^{o}C, results suggest that a 'self-healing' effect involving the precipitation of substantial levels of nano-scale polycrystalline $FeCO_3$ is capable of hindering the growth of active pits in the conditions evaluated. The results also reflect that in instances where high general corrosion rates of the steel surface are observed, the growth rate of pits were heavily underestimated by profilometry measurements (which recorded pit depths relative to the corroded surface). The concept of 'relative' pitting and 'absolute' pitting rates/depths are consequently introduced and the discrepancies between both interpretations are discussed.

KEY WORDS: Carbon dioxide corrosion, iron carbonate, iron carbide, uniform corrosion, pitting.

INTRODUCTION

The problem of corrosion in oilfield environments is predominantly associated with the presence of dissolved gases in reservoir brines such as CO_2 (termed sweet corrosion) and H_2S (termed sour corrosion) [1-4]. Pitting corrosion is one of the main modes of corrosion related failure encountered during oil and gas transportation, playing a significant role on the economics of the production process, influencing both capital (CAPEX) and operating (OPEX) expenditure, as well as the environment [2, 5]. A localized form of attack such as pitting corrosion is of particular concern because of its unpredictable nature and the difficulty associated with inhibiting pit propagation once it has initiated.

Incidences of pitting corrosion failures are becoming increasingly prevalent in oil and gas installations exposed to CO_2/H_2S-saturated brines [6, 7]. The tendency for pits to initiate and

propagate can be influenced by factors such as temperature, *in-situ* pH, exposure time and solution chemistry (e.g. chloride ion concentration) [8-11].

In terms of passive materials, the mechanisms of pitting corrosion are relatively well understood and generally revolve around the localized breakdown of the passive film, leading to the propagation of surface pits [12]. However, what currently remains unclear are the actual mechanism(s) of pitting corrosion in the case of non-passivating materials such as carbon steel in CO_2/H_2S-saturated environments [2, 12-14]. It is essential to understand the initiation and propagation of pits in these particular environments in order to determine when pitting corrosion will become a threat to pipeline integrity and how to mitigate it effectively [11, 15].

The research presented within this publication focuses on exploring the effect of temperature as a primary factor, as well as other secondary factors (solution chemistry, pH and corrosion product characteristics), on the pitting corrosion of X-65 steel in CO_2-saturated brines. These particular tests were performed within unbuffered solutions with the view of elucidating the synergy of how environmental variables may influence the mechanism of pitting corrosion in oilfield environments. The paper intends to contribute towards the literature by offering a more comprehensive understanding of the influence of temperature and the associated secondary parameters which temperature affects (particularly corrosion product morphologies and their evolution) on pitting corrosion. The research is aimed at improving the existing understanding of the mechanism of pitting corrosion of carbon steels in CO_2-saturated environments.

EXPERIMENTAL PROCEDURE

Materials: X-65 carbon steel samples were used as the working electrodes within a three-electrode cell in every experiment. The steel was in a normalized form and consequently possessed a ferritic/pearlitic microstructure. The nominal composition of the X-65 steel is provided in Table 1.

Table 1: X-65 carbon steel elemental composition (wt.%)

C	Si	P	S	Mo	Ni	Nb	V	Mn	Fe
0.15	0.22	0.025	0.002	0.17	0.09	0.054	0.057	1.422	97.81

The steel was sectioned into 10 mm x 10 mm x 5 mm samples and wires were subsequently soldered to the back of each test specimen before embedding in a non-conducting resin. Prior to the start of each experiment, samples were wet ground up to 1200 silicon carbide grit paper, degreased with acetone, rinsed with distilled water and dried with compressed air before immersion into the test solution. A surface area of 1 cm^2 was exposed to the electrolyte per sample.

Brine preparation and solution chemistry: A 10 wt.% NaCl brine solution was used for all experiments. A glass vessel containing two (2) liters of the test solution was saturated with CO_2 for a minimum of 12 hours prior to starting each experiment to reduce oxygen concentration down to 20 ppb, simulating oilfield environments. CO_2 was bubbled into the system throughout the duration of every experiment. The partial pressures at each temperature were determined using Raoult's law and the associated data is provided in Table 2 for the test temperatures of 30, 50 and 80°C. All vapour pressure data were obtained from handbooks of thermodynamic properties for substances[16]. All tests were conducted at atmospheric pressure.

Table 2: Approximate partial pressures of CO_2 in a 10 wt.% NaCl solution at the experimental temperatures considered

Temperature (°C)	p_{CO2} (bar)
30	0.97
50	0.90
80	0.57

In-situ electrochemical measurements and test procedure: The working electrodes (carbon steel samples) were used in a three-electrode cell which also comprised of an Ag/AgCl reference electrode and a platinum auxiliary electrode. Corrosion rate measurements were conducted in the form of DC linear polarization resistance (LPR) measurements over the duration of each experiment, using an ACM Gill 8 potentiostat. The working electrode was polarized ±15 mV about the open circuit potential (OCP) at a scan rate of 0.25 mV/s. Tafel constants used for the corrosion rate calculation were estimated from Tafel polarization tests conducted on freshly polished samples in separate tests at each temperature to ensure reliable data collection for accurate estimation of uniform corrosion rate.

Table 3 outlines the Tafel constants measured, which were obtained by performing anodic and cathodic sweeps ±250 mV about the OCP at a scan rate of 0.25 mV/s.

Table 3: Tafel constants at different temperatures for freshly polished X-65 steel exposed to a 10 wt.% NaCl CO_2-saturated solution

Temperature (℃)	β_a (mV/decade)	β_c (mV/decade)	B (Stern-Geary coefficient) (mV/decade)
80	75	140	21.21
50	55	160	17.77
30	43	180	15.07

For each long term experiment, 10 samples were initially placed into each of the two liter test vessels. Two samples were subsequently removed from each test cell at sampling times of 7, 36, 72, 120 and 168 hours to enable the evolution of corrosion products and the growth of surface pits to be examined. LPR measurements were conducted on two samples per test cell for the entire test duration to allow collection of electrochemical data over the full 168 hours of exposure. All tests were performed in static conditions.

When samples were removed from the test cell they were gently rinsed with distilled water and dried with compressed air. All samples were preserved under vacuum in a desiccator prior to post-experiment surface analysis. Samples used for pitting analysis were cleaned with Clarke's solution (20 g antimony trioxide + 50 g stannous chloride and hydrochloric acid to make 1000 ml) to remove all traces of corrosion products in accordance with ASTM Standard G1-03 [17]. Duplicate experiments were conducted concurrently to ensure repeatability and to enable validation of all results. A schematic of the static bubble cell experimental setup is provided in Figure 1.

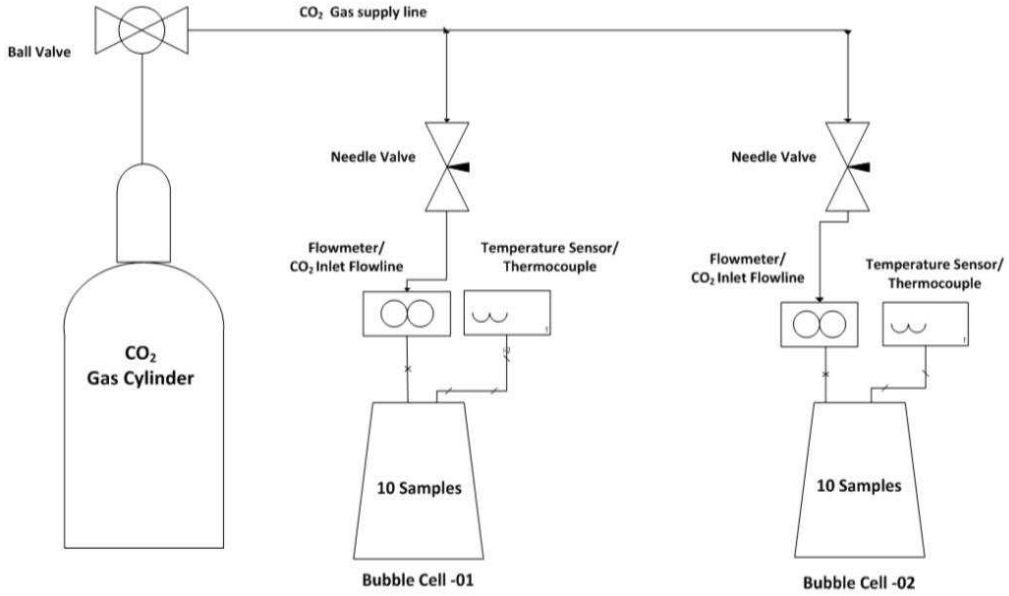

Figure 1: Schematic of the static bubble cell setup used for CO_2 corrosion testing

The focus of this study is to investigate the temperature effect on pitting corrosion. Corrosion testing was conducted for 168 hours in static conditions with the aim of monitoring pit growth throughout the entire experiment. The work predominantly evaluates the effect of temperature, but also takes into account changes in secondary parameters such as pH and corrosion product formation (as a result of the temperature changes) and the corresponding effect these parameters have on the overall pitting corrosion behavior of carbon steel. Electrochemical responses (implementing the LPR technique) are also evaluated with the purpose of relating changes in general corrosion rate to the propagation of localized attack.

Surface characterization: X-ray diffraction (XRD) patterns were obtained using a PHILIPS X'PERT X-ray diffractometer. XRD data collection was based on 2-Theta scans in grazing angle geometry. Scanning electron microscopy (SEM) analysis was performed using a ZEISS EVO MA 15. An energy dispersive X-ray (EDX) detector was coupled to the SEM for determination of the elemental composition of various corrosion products. Raman analyses were conducted using a Renishaw inVia microscope on a 488 nm wavelength laser. Spectra were obtained using 0.5 mW laser power at 1 s exposure time. 50 accumulations were obtained to increase the signal to noise ratio.

Characterization of pitting corrosion damage: Pit depth measurements were conducted in alignment with ASTM G46-94 [18]. An NPFLEX 3D interferometer was used in this study to define the discrete geometry of cavities on almost the entire steel sample surface. Pit cavities were identified based on carefully chosen thresholds which allow distinct pit depths, diameters and areas to be accurately quantified. ASTM G46-94 stipulates that an average of the 10 deepest pits and the maximum pit depth (based on pit depth measurement after removal of corrosion products) should be used for pit damage characterization for the sample area. A surface area of 9 x 9 mm^2 was analyzed for pits from the 10 x 10 mm^2 sample surface. A systematic stitching approach is then adopted whereby 9 different 3 x 3 mm^2 areas are stitched together. Consequently, 3D images of regions where the deepest pits exist are identified on the sample surface with a high degree of accuracy and resolution.

It is very important to note that there is no generally accepted consensus on the minimum dimensions a pit can take in terms of depth and diameter, especially in non-passivating alloys like carbon steels. However, there are various suggestions of the different possible shapes, orientations

and sizes of pits in ASTM G46-94 [18]. Nonetheless, attempts have been made in this work to give visual evidence of pits/cavities in terms of the largest pits identified by the techniques used in this work and consequently, examples are provided in Figure 2.

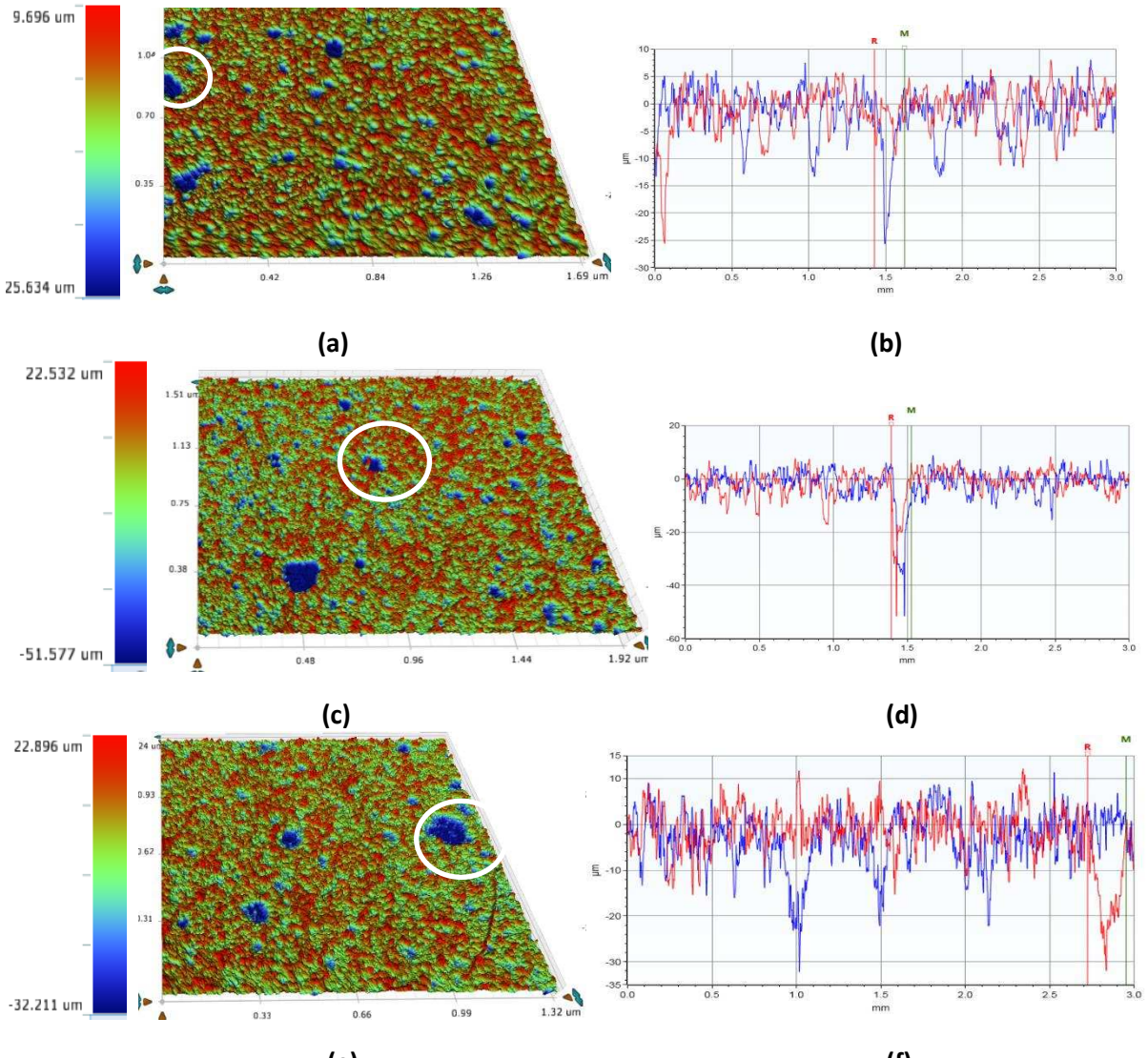

Figure 2: Examples of 3D and 2D profiles of measurable maximum pits on the surface of X-65 carbon steel; (a) 3D and (b) 2D at 30°C after 168 hours, (c) 3D and (d) 2D at 50°C after 168 hours and (e) 3D and (f) 2D at 80°C after 168 hours exposed to a 10 wt. % NaCl solution saturated with CO_2.

An important parameter applied in the characterization of pitting corrosion damage is the pitting factor (P_f), which is used to reflect the relative contribution of degradation between uniform and pitting corrosion and is defined in ASTM G46-94 [18] as:

$$P_f = \left(\frac{P_d}{P_u}\right) = \left(\frac{P_u + d_{max}}{P_u}\right) \quad (1)$$

Where P_d is the 'absolute' pit depth (the sum of the 'relative' pit depth to the corroded surface (d_{max}), plus the average metal penetration from general corrosion rate measurements (termed P_u), i.e. $P_d = P_u + d_{max}$). Values are usually referred to in µm and d_{max} can be determined through profilometry measurements of the steel surface after cleaning, whilst values of P_u can be quantified

by converting the average LPR corrosion rate into a general thickness loss based on the exposure time of the sample to the test solution.

A pitting factor of 1 represents uniform corrosion. The greater the pitting factor, the greater the depth of penetration relative to the surrounding surface area.

Another parameter considered in this study is the absolute pit penetration rate (in mm/year), which were determined based on the increase in the pit depths (d_{max} and P_d) recorded as a function of time over each sampling time interval. By measuring the pit depth between samples and considering the time between each sample removal, it was possible to determine the rate at which pits were growing both in absolute terms and relative to the surrounding corroded area.

RESULTS AND DISCUSSION

Corrosion product formation at 30°C: This section discusses the relationship between the electrochemical activities at the metal-brine interface and the different stages of corrosion product formation, including networks of iron carbide (Fe_3C) often revealed after the preferential dissolution of the ferrite phase. Figure 3 shows the electrochemical behavior (OCP and LPR corrosion rate) of X-65 steel over 168 hours of exposure to the 10 wt.% NaCl solution at 30°C. The different stages of observed corrosion products on the metal surface over the exposure time of 168 hours are also provided in Figure 4 in the form of SEM images, as well as being annotated within Figure 3 itself.

Referring to Figure 3, between 0 and 7 hours of corrosion testing, a steady increase in general corrosion rate and ennoblement of OCP are apparent. The marked increase in OCP is in alignment with the revealing of an Fe_3C layer, as shown in Figure 4(a) and has been observed by several other authors when ferrite preferentially dissolves from the steel surface and no corrosion product precipitation occurs within the system [2, 15, 19]. There is a suggestion in literature that the revealing of this undissolved layer may lead to the accentuated corrosion rate at anodic regions [15, 20]. Such an observation has been suggested to create a galvanic effect between local anodic and cathodic sites of the same steel surface, ultimately leading to the potential accentuation of pitting/localized corrosion [2, 15, 19, 20].

After 36 hours of exposure (Figure 4(b)), the onset of a form of corrosion product (often referred to as an amorphous layer based on other observations in literature [21, 22]) is shown to establish itself on the steel surface and potentially within the voids of the Fe_3C layer. The seemingly amorphous corrosion product layer (believed to be $FeCO_3$ based on extensive energy dispersive X-ray (EDX) measurements which produced elemental ratios of ≈ 1:1:3 for Fe:C:O) was observed to develop into a continuous layer with *very* small traces of nano-scale crystals of $FeCO_3$ existing on top of this layer (highlighted in Region 'A' within Figure 4(b)).

The formation of ‘amorphous’ $FeCO_3$ is made favorable by the low pH of the system and has been previously observed and characterized in literature within similar environments [22, 23]. The period of formation of the amorphous layer also coincides with a transitory stabilization of OCP with a steady increase in general corrosion rate (Figure 3). Adjudging by the SEM images in Figures 4(a) and (b), it is clear that the surface layer is still dominated by Fe_3C during this period, suggesting that the deposition of this corrosion product layer had not been occurring for a particularly long period of time.

Between 36 and 72 hours of immersion there was an apparent increase in the quantity and coverage of the amorphous $FeCO_3$ layer. The morphology of the corrosion product layer shown in Figure 4(c) indicated the slight presence of nano-scale crystals growing together on top of the amorphous layer. This period of immersion is marked by continued increase in general corrosion rate and a slight

increase in OCP of the steel. The increase observed could be related to galvanic effects between Fe_3C and the steel surface, as suggested by Crolet et al [15], but cannot be proven. What is evident though is that the presence of the different corrosion product morphologies observed at this stage (Fe_3C and amorphous/nano-crystalline $FeCO_3$) is having little or no effect on reducing the *general* corrosion rate of the underlying steel.

From 72 hours onwards, a marginal increase in general corrosion rate is observed, followed by a subsequent reduction after almost 150 hours. The corrosion product layer formed on the steel sample at this time is dominated by amorphous $FeCO_3$, as well as traces of more nano-scale crystals whose composition is indicative of the presence of $FeCO_3$ on the XRD patterns provided in Figure 5 which can be compared to the reference patterns of Fe, Fe_3C and $FeCO_3$ shown in Figure 6 [24].

The results may suggest that the precipitation of amorphous and/or nano-polycrystalline $FeCO_3$ could have the ability to offer small amounts of protection to the general corrosion rate of the steel surface towards the end of this particular test. However, it could also be suggested that the pH change of the bulk solution from 4.85 to 5.00 may also have helped suppress general corrosion rate through reduction of the cathodic reaction, and this fact cannot be discounted [25]. Regardless of this effect, the change is only slight and it can be confirmed that no substantial level of protection is offered by the corrosion product layer.

It is worth noting that the XRD pattern of the sample exposed to the electrolyte for 168 hours provided in Figure 5 suggest the presence of crystalline $FeCO_3$ (a corrosion product known to offer protection to the steel surface through either blocking active sites on the steel surface or acting as a diffusion barrier to electrochemically active species involved in the cathodic reaction) [2]. However, the extent and mode of precipitation was not adequate enough or suitable to significantly influence the general corrosion behaviour of the underlying steel substrate. The XRD pattern provided in Figure 5 also show peaks at 34.9 and 56.1 2theta to suggest the presence of the compound Iron Molybdenum Oxide (Fe_2MoO_4) [26]. This compound is likely due to the presence of molybdenum as an alloying element in steel chemistry.

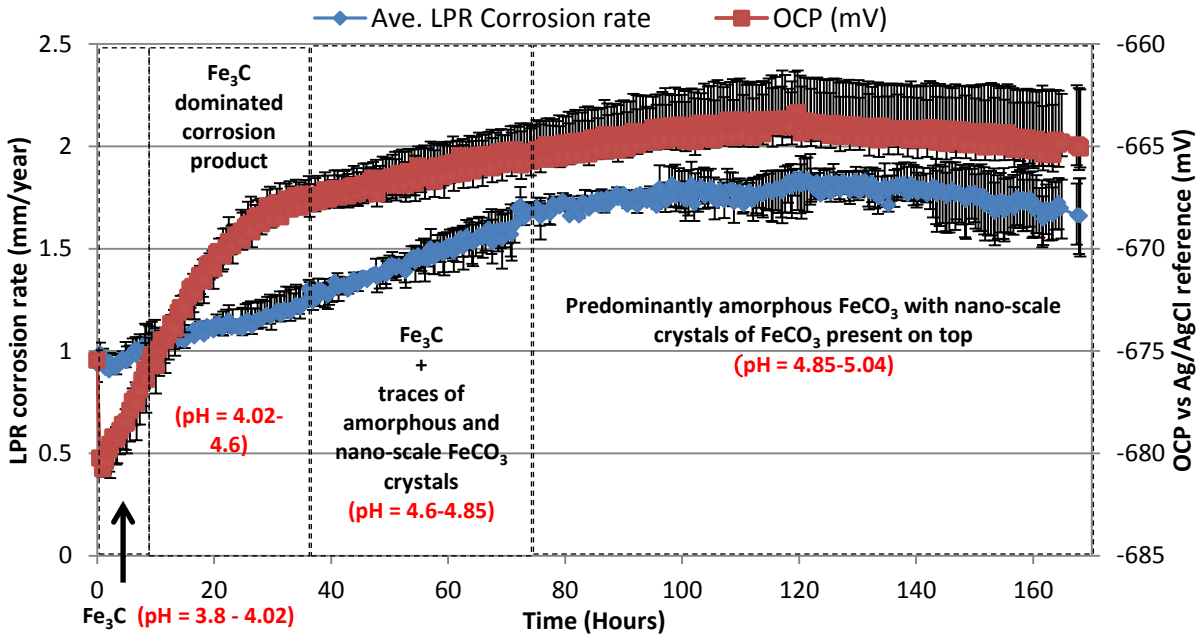

Figure 3: A plot of LPR corrosion rate and open circuit potential of X-65 steel over a duration of 168 hours in a 10 wt. % NaCl solution saturated with CO_2 at 30°C

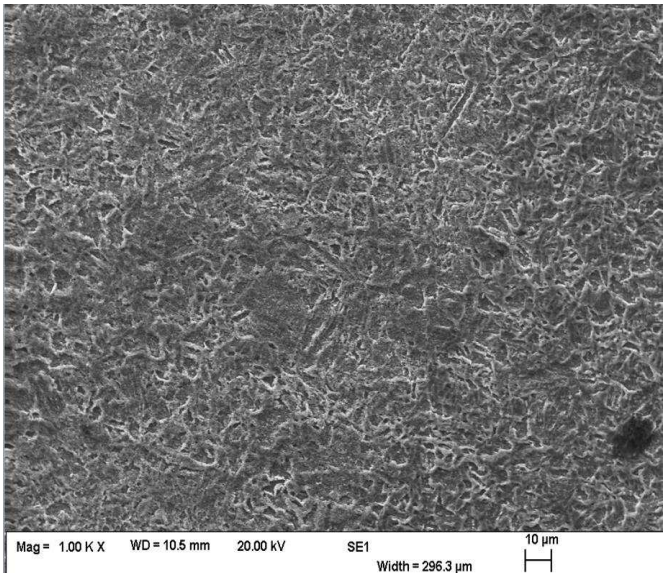
Mag = 1.00 K X
WD = 10.5 mm
20.00 kV
SE1
Width = 296.3 µm
10 µm

(a)

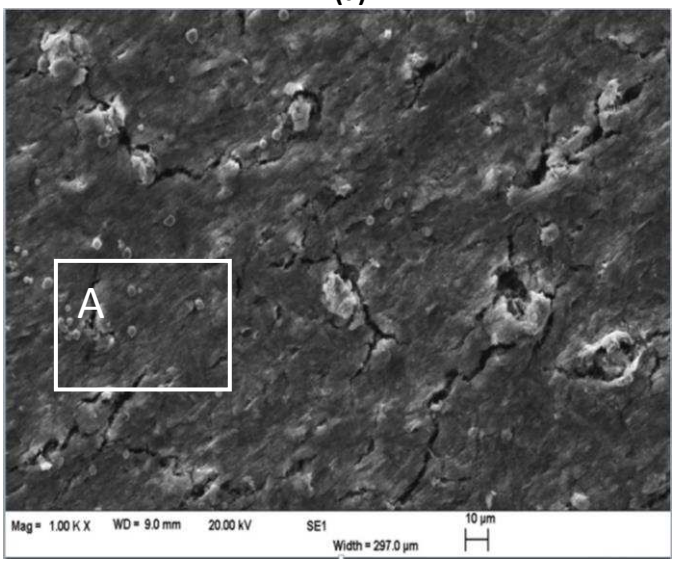
A
Mag = 1.00 K X
WD = 9.0 mm
20.00 kV
SE1
Width = 297.0 µm
10 µm

(b)

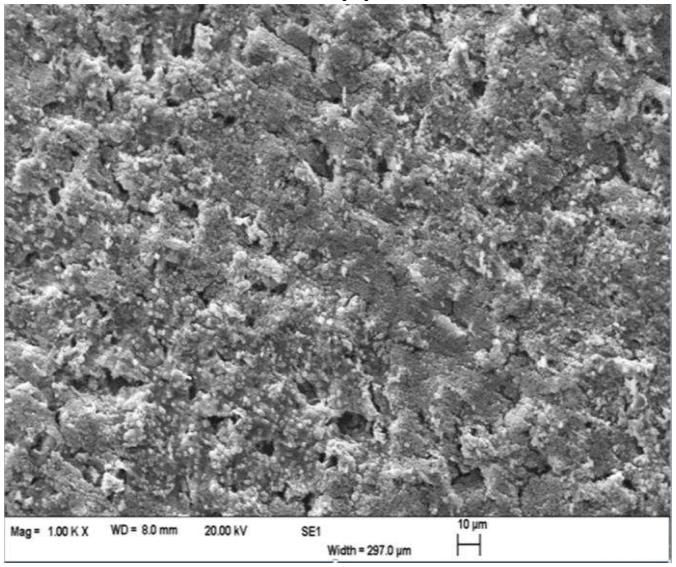
Mag = 1.00 K X
WD = 8.0 mm
20.00 kV
SE1
Width = 297.0 µm
10 µm

(c)

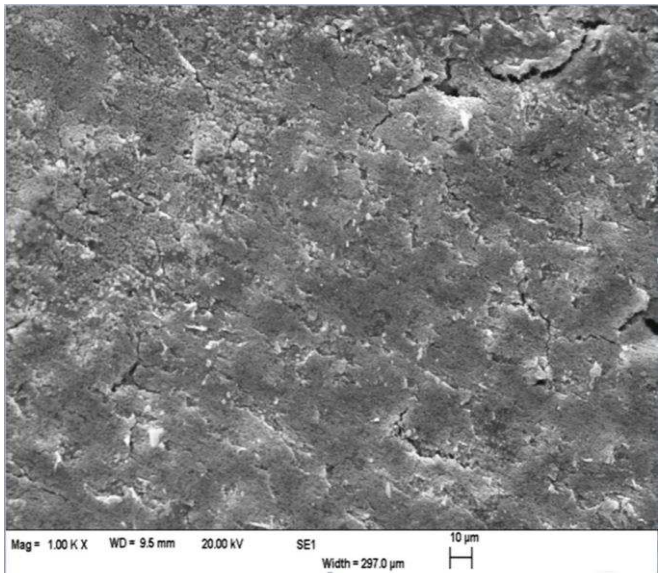

(d)

Figure 4: SEM images of corrosion product on X-65 samples exposed to 10 wt.% NaCl solution saturated with CO_2 at 30°C (a) 7 hours, (b) 36 hours, (c) 72 hours and (d) 168 hours

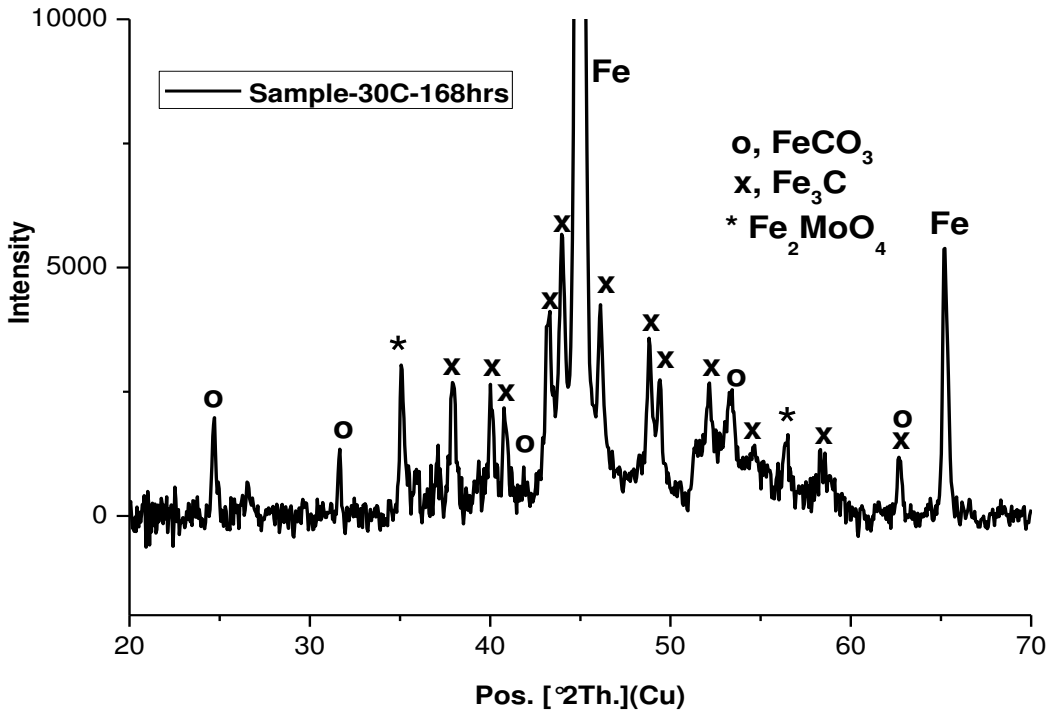

Figure 5: XRD pattern for corrosion product on X-65 steel after 168 hours at 30°C (SEM image of Figure 4(d)). (Note that the intensity scale is arbitrary)

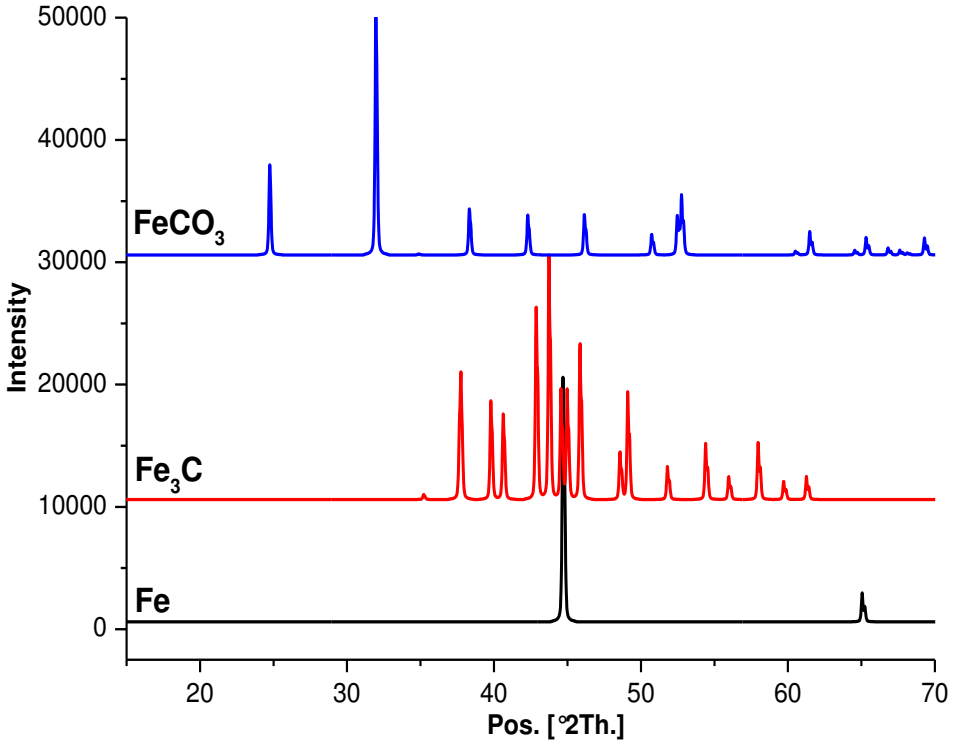

Figure 6: Reference XRD patterns for Fe, Fe_3C and $FeCO_3$ [27-30]

Pitting corrosion behavior of carbon steel at 30°C: Over the course of the experiment performed at 30°C, relatively continuous pit growth was observed, from maximum depths of 4.1 µm after 7 hours, up to 25.6 µm after 168 hours, as shown in Figure 7. However, between 36 and 72 hours, pit growth rate was only marginal. The reduction in pit growth rate shown in Figure 7 may be attributed to the accelerated level of general corrosion which occurs in this region (referring back to Figure 3 between 36 and 72 hours). It is important to note that the pit depths presented in Figure 7 are depths relative to the corroded surface. Consequently, if general corrosion rate increases and pit growth remains constant, the *relative* growth of pits appears to slow down.

Over the initial stages of exposure, the pits formed on the steel surface are very shallow (< 15 µm) and thus could significantly be masked by the general corrosion rate contribution to total thickness loss. Unlike passive materials, a substantial level of general corrosion exists throughout the test in conjunction with the growth of the pit on the surface. Such a contrasting mode of corrosion damage could be underplaying the fact that pits are actually still continuously growing despite the small increase in pit depth measured. This aspect is discussed in detail later.

Finally, for the tests at 30°C, pit growth continues between 72 and 168 hours, indicating that the presence of amorphous $FeCO_3$ on top of the Fe_3C network has little or no effect in terms of inhibiting pit propagation. Instead there is a possibility that the Fe_3C layer may even promote pitting corrosion on other localized anodic regions through a galvanic effect.

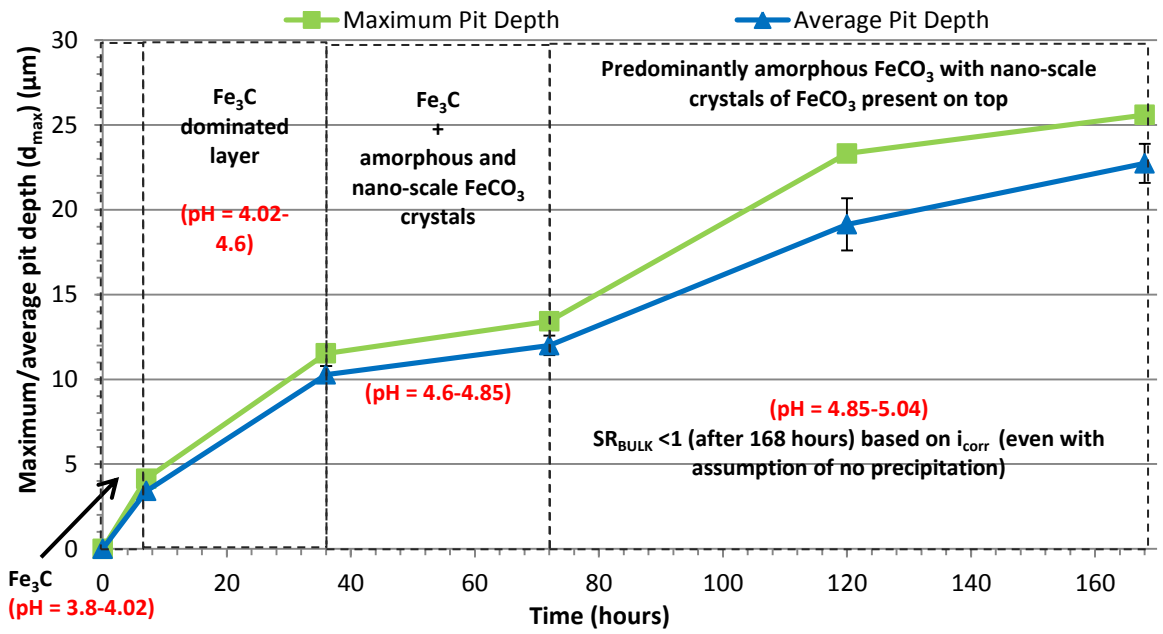

Figure 7: Plot depicting the variation of relative pit depth (maximum and average) with time at 30°C, over a duration of 168 hours in a 10 wt.% NaCl solution saturated with CO_2. Error bars represent the standard deviation based on the 10 deepest pits.

Corrosion product formation at 50°C: The variation in general corrosion rate and OCP over the course of the 168 hours experiment at 50°C is provided in Figure 8. The surface layer consists of a network of Fe_3C between 0 to 7 hours at 50°C which was produced by the fast rate of preferential ferrite dissolution. The formation of such a corrosion product layer is supported by a rapid increase in both OCP and general corrosion rate, as depicted in Figure 8. The rise in OCP observed with corrosion rate is likely to be attributed to an increase in the cathodic reaction as a result of more Fe_3C sites progressively revealing themselves [2, 8, 15]. The rate of increase in corrosion rate and potential is much faster than that observed at 30°C, suggesting a quicker rate of revealing of the Fe_3C network. Between 7 and 36 hours, the general corrosion rate continues to increase rapidly and peaks after 30 hours, coinciding with stabilization of the OCP.

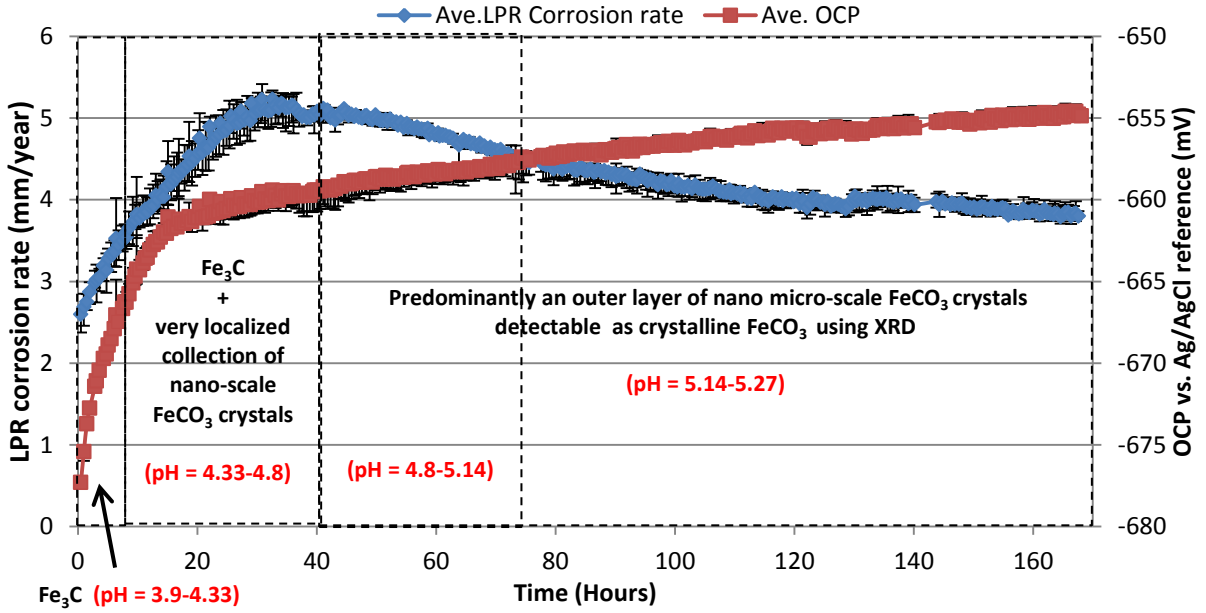

Figure 8: A plot of LPR corrosion rate and open circuit potential of X-65 steel over a duration of 168 hours in a 10 wt.% NaCl solution saturated with CO_2 at 50°C.

The point at which general corrosion rate begins to reduce coincides with evidence of the deposition of traces of localized agglomerations of $FeCO_3$ crystals (SEM images shown in Figures 9(a) to (d)), which become more evident with time. As stated previously, similar observations of nano-scale $FeCO_3$ crystals were recorded at 30°C but did not appear as quickly as at 50^{o}C, reflecting the effect of increasing temperature on the rate of formation of such corrosion products.

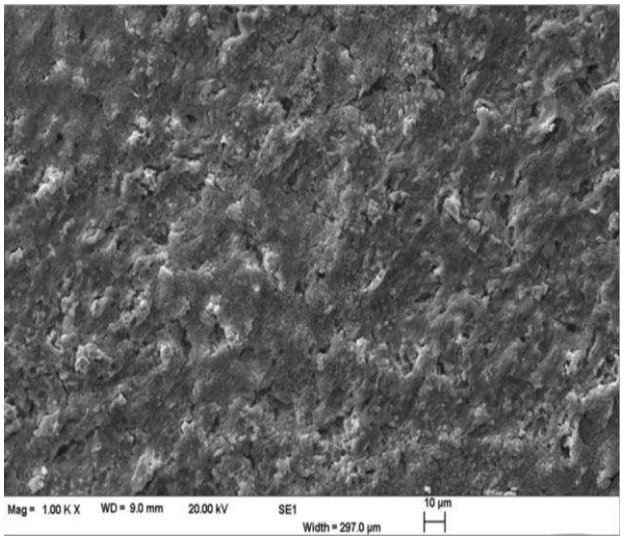

(a)

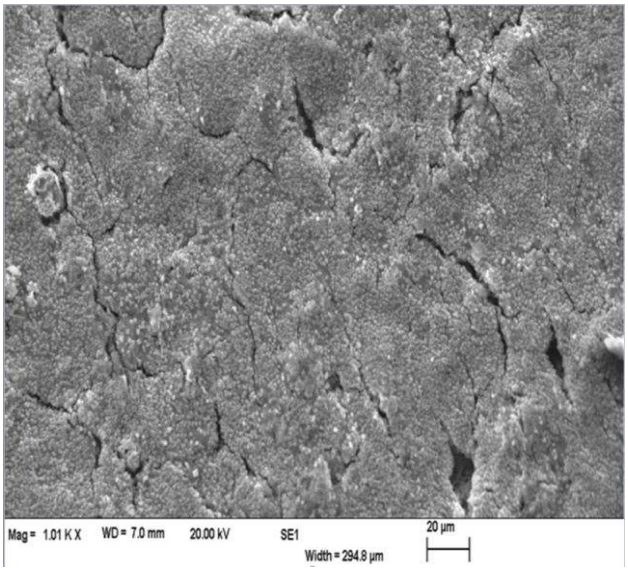

(b)

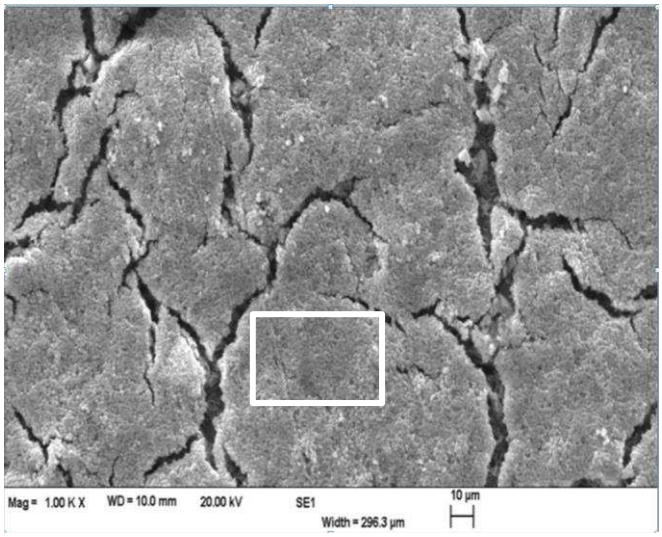

(c)

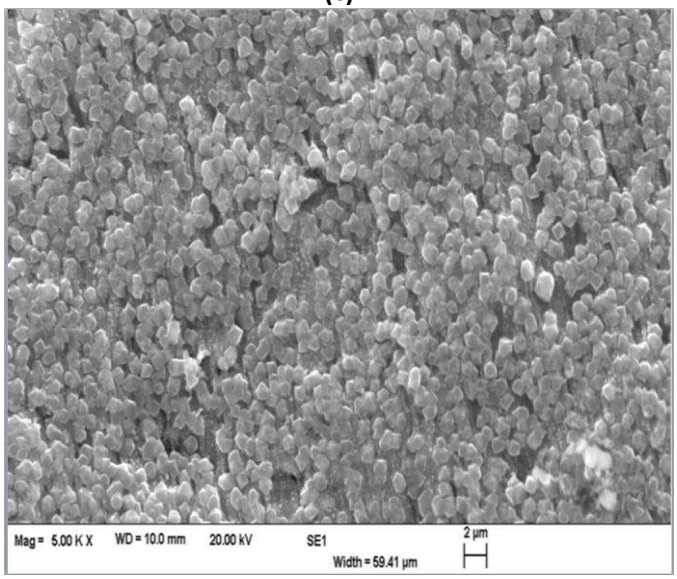

(d)

Figure 9: SEM images of corrosion product on X-65 samples exposed to 10 wt.% NaCl solution saturated with CO_2 at 50°C (a) 36 hours, (b) 72 hours, (c) 168 hours and (d) magnified image of region identified in (c)

Between 36 and 72 hours, the $FeCO_3$ crystal size becomes larger, occupying a greater proportion of the steel surface (Figure 9(b)). The crystal initiation and growth process coincides with a gradual reduction of corrosion rate and increase in OCP. This behavior was also observed up to the end of the test and could be influenced by a relatively higher pH than at 30°C, leading to a higher nucleation and growth rate of $FeCO_3$ crystals.

The reduction in general corrosion rate in Figure 8 from 30 hours onwards could be partially attributed to the increase in pH observed over this period (4.8 to just over 5.14 after 168 hours). However, a reduction in general corrosion rate with a steady *increase* in OCP suggests suppression of anodic reaction relative to cathodic process, which could potentially be linked to the blocking of active sites (although only slight) on the surface by the precipitation of $FeCO_3$. As stated previously, an increase in surface pH typically leads to a drop in OCP by reducing the rate of the overall cathodic reaction [31].

The XRD pattern of the X-65 sample surface after 168 hours (shown in Figure 10) indicates strong peaks for $FeCO_3$, confirming the substantial presence of crystals deposited on the surface of the steel relative to those observed at 30°C. Figure 9(d) shows the developed crystals on the steel surface clearly, which possess an average diameter of approximately 1 µm. There are also peaks at 29.7, 34.9 and 56.1 2theta to suggest the presence of the compound Iron Molybdenum Oxide (Fe_2MoO_4) at this temperature [26].

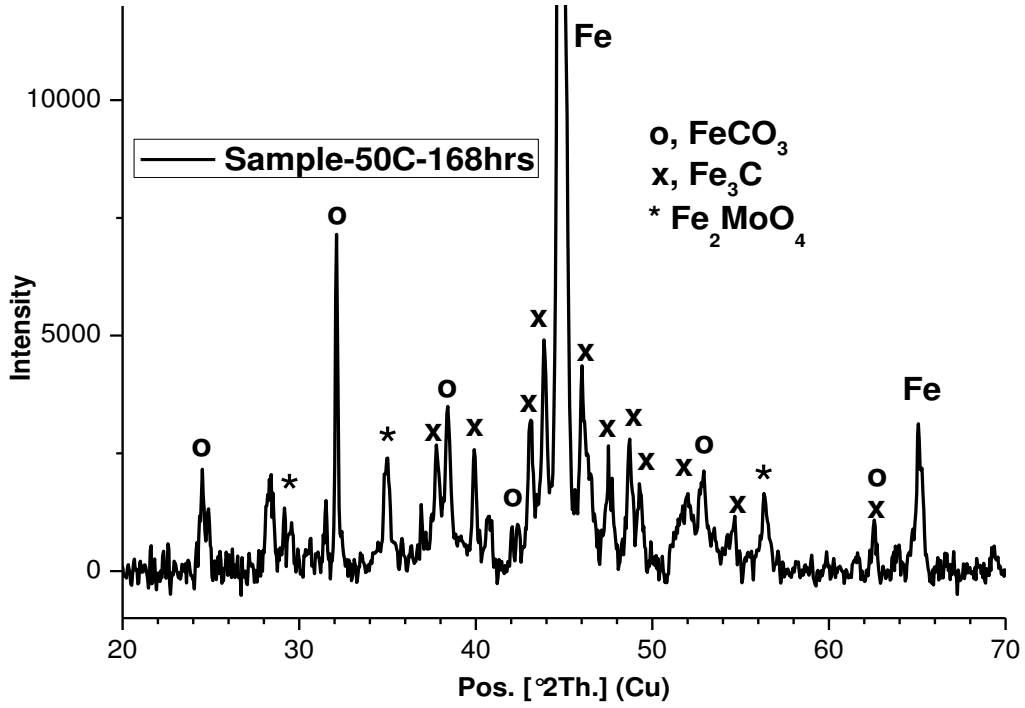

Figure 10: XRD pattern for corrosion product on X-65 steel after 168 hours at 50°C (SEM image in Figure 9(d)). (Note that the intensity scale is arbitrary)

Pitting corrosion behavior of carbon steel at 50°C: Referring to Figure 11, once pits initiate as recorded after 7 hours, there is an observed steady and almost linear growth rate of pits from 8.2 µm after 7 hours up to 52.5 µm after 168 hours. Most importantly, despite the evidence of the formation of a crystalline $FeCO_3$ outer layer, the role of this particular corrosion product morphology and/or corrosion environment on reducing general corrosion rate appears not to have the same influence on the ability of pits to propagate. The fact pit growth continues unhindered may be due to the non-uniform coverage of $FeCO_3$ crystals on steel surface. Furthermore, any potential galvanic effects between Fe_3C regions and exposed areas of localized pores and the associated corrosion kinetics would be enhanced by the higher temperature, leading to the more substantial pit growth process at 50°C compared to 30°C. Such behavior is consistent with observations by other authors [22, 23].

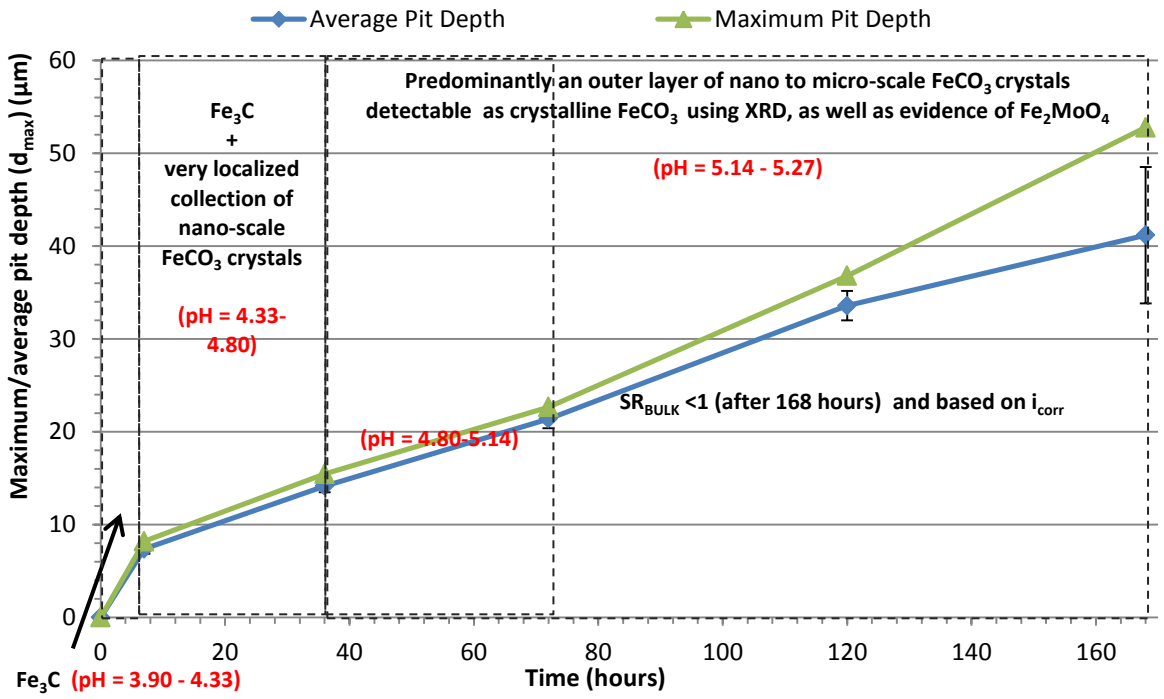

Figure 11: Plot depicting the variation of relative pit depth (maximum and average) with time at 50°C, over a duration of 168 hours in a 10 wt.% NaCl solution saturated with CO_2. Error bars represent the standard deviation based on the 10 deepest pits.

Corrosion product formation at 80°C: The general corrosion rate, OCP and corrosion product formation observed throughout the test at 80°C is presented in Figure 12. The corrosion behavior is characterized by a very rapid increase in general corrosion rate and OCP between 0 and 7 hours. General corrosion rate peaks at about 11 hours while the corresponding effect of this is the evidence of a layer which consisted of an agglomeration of nano-scale $FeCO_3$ crystals which were visible after only 7 hours of immersion and similar to those recorded at 50°C beyond 36 hours (Figure 9(d)). The corrosion product became distinctly more visible after 36 hours and is shown within Figure 13(a) as a layer exhibiting a smudge-like texture.

Based on the ratio of uniform corrosion rate at start of each test to when it peaks at each respective temperature, the revealing of Fe_3C at 50°C appears to be having the greatest effect on corrosion rate i.e. the ratio of peak corrosion rate to initial corrosion rate for each temperature was largest at 50°C. However, in terms of the actual magnitude of uniform corrosion rate, an increase of approximately 2.5 mm/year from the initial corrosion rate is observed at both 50°C and 80°C, while there is only an increase of 1 mm/year at 30°C, indicating that the revealing of the Fe_3C network had a greater effect on increasing corrosion rates at higher temperatures in these particular experiments.

Between 7 and 36 hours at 80°C, uniform corrosion rate starts to reduce, whilst OCP increases (Figure 12) in conjunction with the formation of a top layer of amorphous $FeCO_3$ above the Fe_3C network based on SEM images (Figure 13(a)). The observed decrease in corrosion rate at this time could potentially be linked to increasing pH from 5.00 to 5.60. However, continuous increase in potential suggests that some of the active corrosion sites are being blocked as a result of $FeCO_3$ formation. Continuous reduction in corrosion rate was also observed between 36 and 72 hours, even while the potential appears to be relatively stable. This also coincides with evidence of further formation of crystalline $FeCO_3$, which is verified from the XRD pattern provided in Figure 14(a).

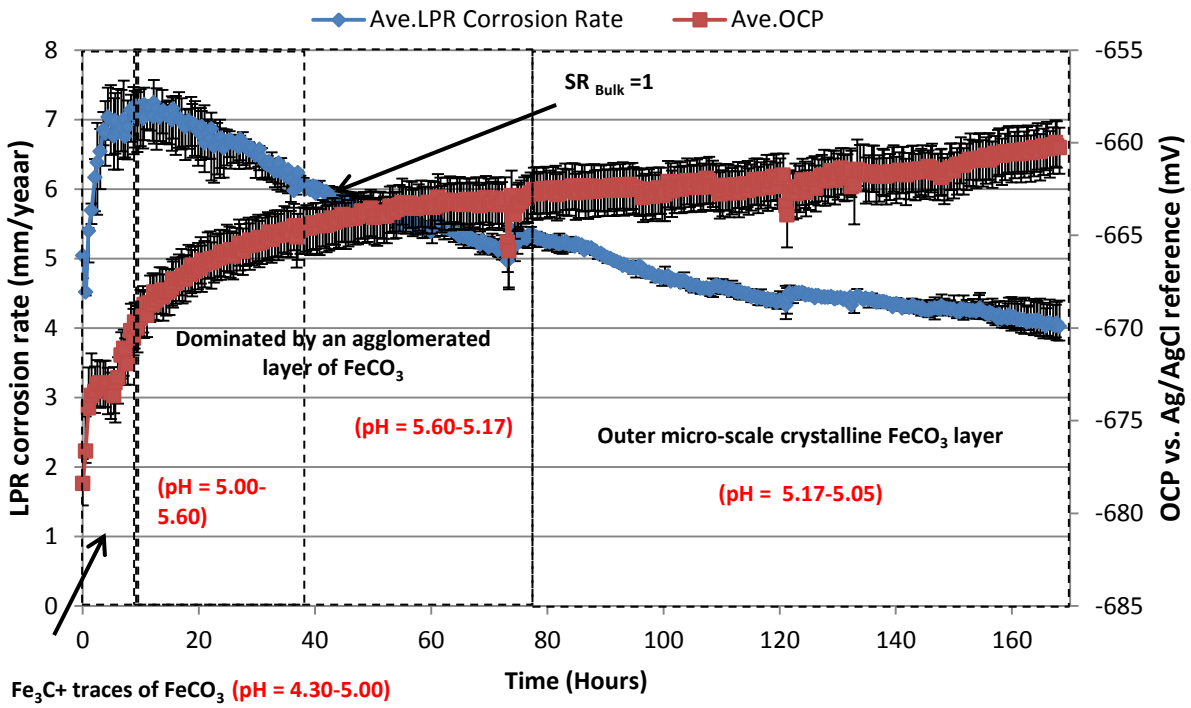

Figure 12: A plot of LPR corrosion rate and open circuit potential of X-65 steel over a duration of 168 hours in a 10 wt.% NaCl solution saturated with CO_2 at 80°C

From 72 hours onwards, OCP stabilizes in conjunction with a marginal increase (followed by a steady decline) in general corrosion rate. Evidence of the presence of crystalline $FeCO_3$ became stronger after 168 hours on the XRD pattern (Figure 14(a)) and within the SEM images (Figure 13(d)) despite the low measured pH of 5.05. Again, regions which appeared amorphous in nature could also be clearly identified. The observations at this stage were also consistent with evolution of $FeCO_3$ corrosion product on steel at 80°C and at pH 6.8 as observed by Ingham et al [32] and Guo et al [22].

To supplement the XRD patterns, Raman spectra of the crystalline and amorphous regions on the steel surface shown in Figure 13(c) and (d) were collected and are provided in Figure 14(b). Both spectra exhibit a strong peak at 1086cm^{-1} and a second diagnostic peak for siderite is at 300 cm^{-1}, indicative of $FeCO_3$ [33, 34].

Referring back to Figure 12, theoretically, a decrease in pH in the bulk solution from 5.6 to 5.05 from 36 to 168 hours would have implied an increase in corrosion rate [2]. However, corrosion rate tends to decrease over this period, most likely because of the formation of $FeCO_3$ [35].This is also supported by the fact that the saturation ratio from corrosion rate measurement in the bulk approaches unity just after 36 hours based on calculations on the average dissolution rate of the X-65 over this period and assuming no significant precipitation occurs prior to this point.

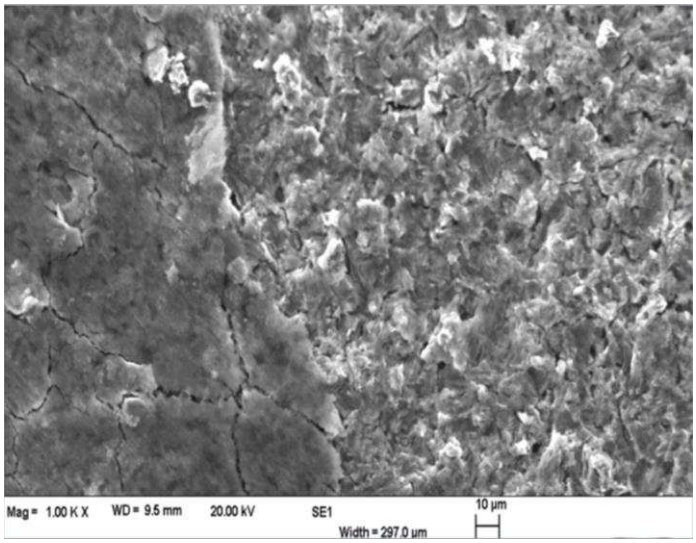
Mag = 1.00 K X
WD = 9.5 mm
20.00 kV
SE1
Width = 297.0 µm
10 µm

(a)

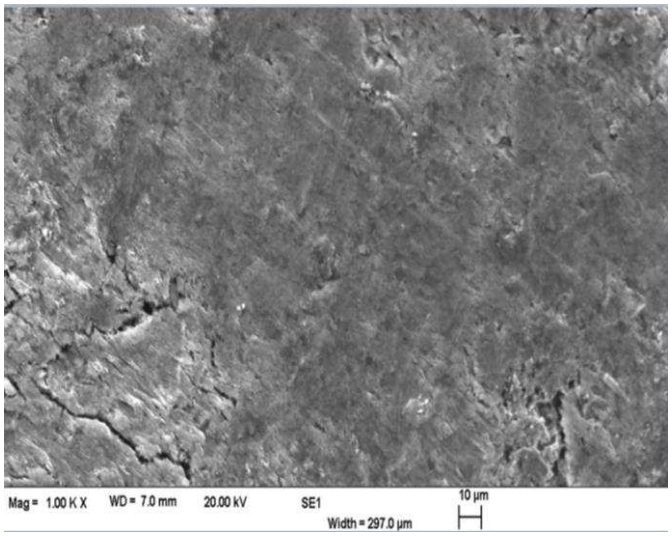
Mag = 1.00 K X
WD = 7.0 mm
20.00 kV
SE1
Width = 297.0 µm
10 µm

(b)

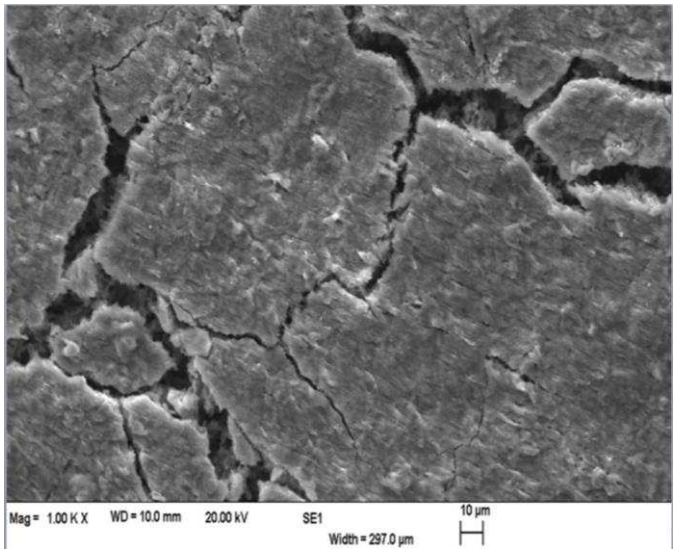
Mag = 1.00 K X
WD = 10.0 mm
20.00 kV
SE1
Width = 297.0 µm
10 µm

(c)

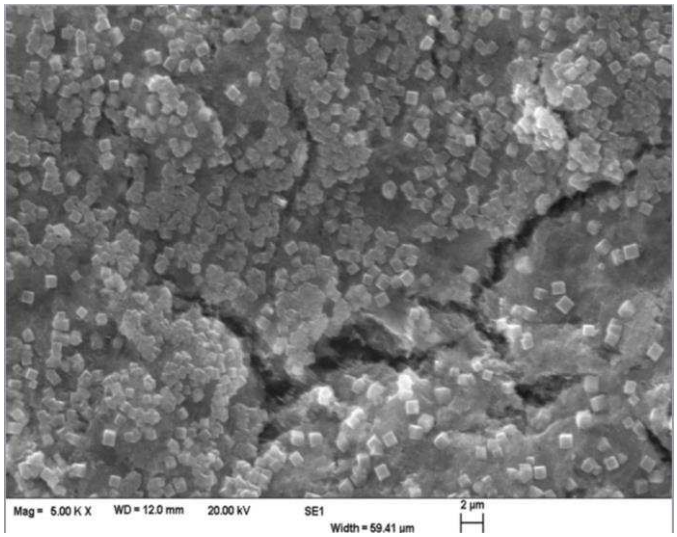

(d)

Figure 13: SEM images of corrosion product above X-65 samples exposed to 10 wt.% NaCl solution saturated with CO_2 at 80°C (a) 36 hours, (b) 72 hours, (c) 168 hours (d) $FeCO_3$ crystals on a different region of sample shown in (c)

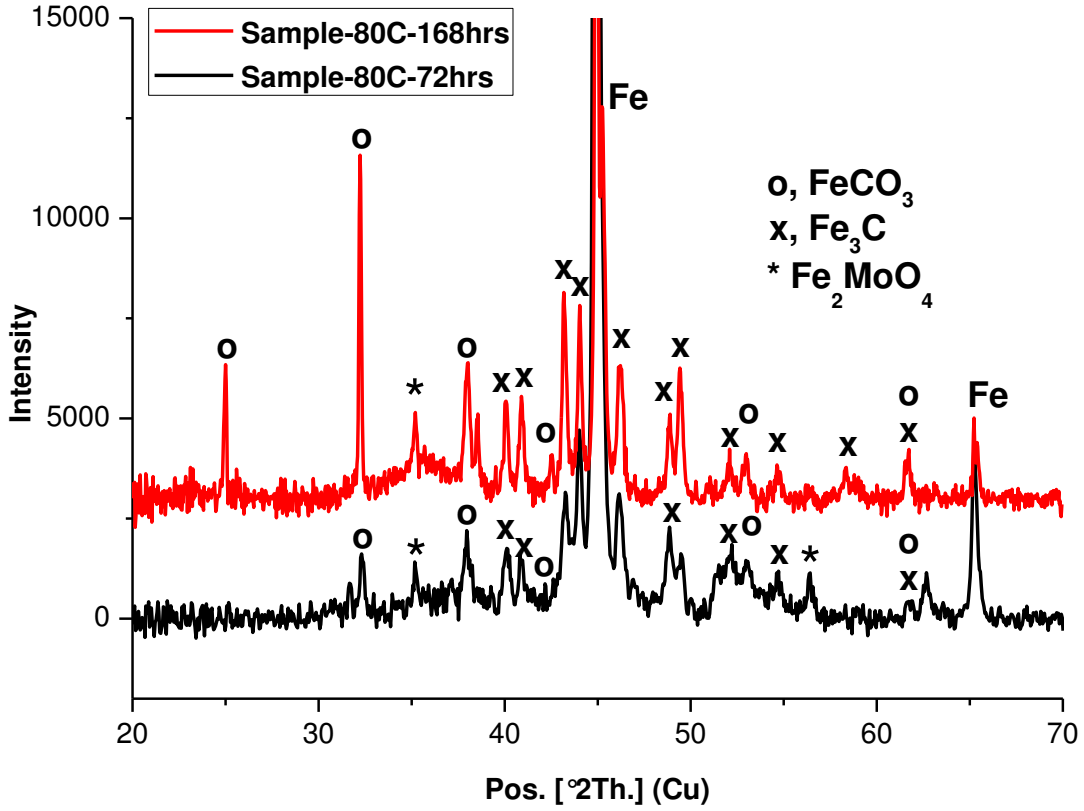

(a)

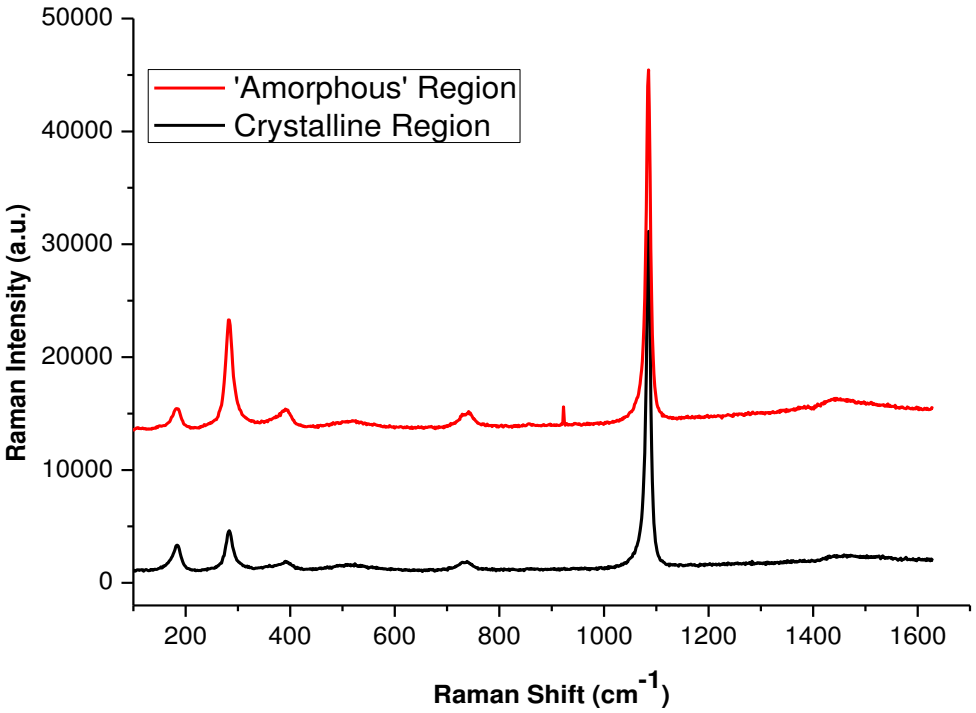

(b)

Figure 14: (a) XRD patterns for corrosion product on X-65 steel after 72 and 168 hours at 80°C (SEM images in Figures 13(b) and 13(d)) and (b) Raman spectra for corrosion product on X65 steel after 168 hours at 80°C on crystalline layer and amorphous inner layer only where no crystalline deposits were located. (Note that the intensity scale is arbitrary)

Pitting corrosion behavior of carbon steel at 80°C: Stable growth of the pits was observed between 0 and 36 hours once pits initiated (shown in Figure 15). Over this stage, the nature of the corrosion product layer comprises of Fe_3C and very small crystals of $FeCO_3$. At some point between 36 and 72 hours where SR_{bulk} (calculated from the rate of dissolution of Fe to Fe^{2+}) equals unity, precipitation of $FeCO_3$ becomes thermodynamically feasible. After the 72 hour mark a distinct reduction in pit growth rate is observed.

Referring back to Figure 12, the rate of general corrosion rate also decreases between 36 and 72 hours, making it less likely for the pit growth rate to be underestimated, while at the same time suggesting a possible healing effect of initially active pits. Crystalline $FeCO_3$ is also detected on the XRD pattern as a weak signal in Figure 14 at 72 hours, which indicates that the presence of $FeCO_3$ crystals may be playing a major role in the reduction of both the growth of pits and general corrosion rate.

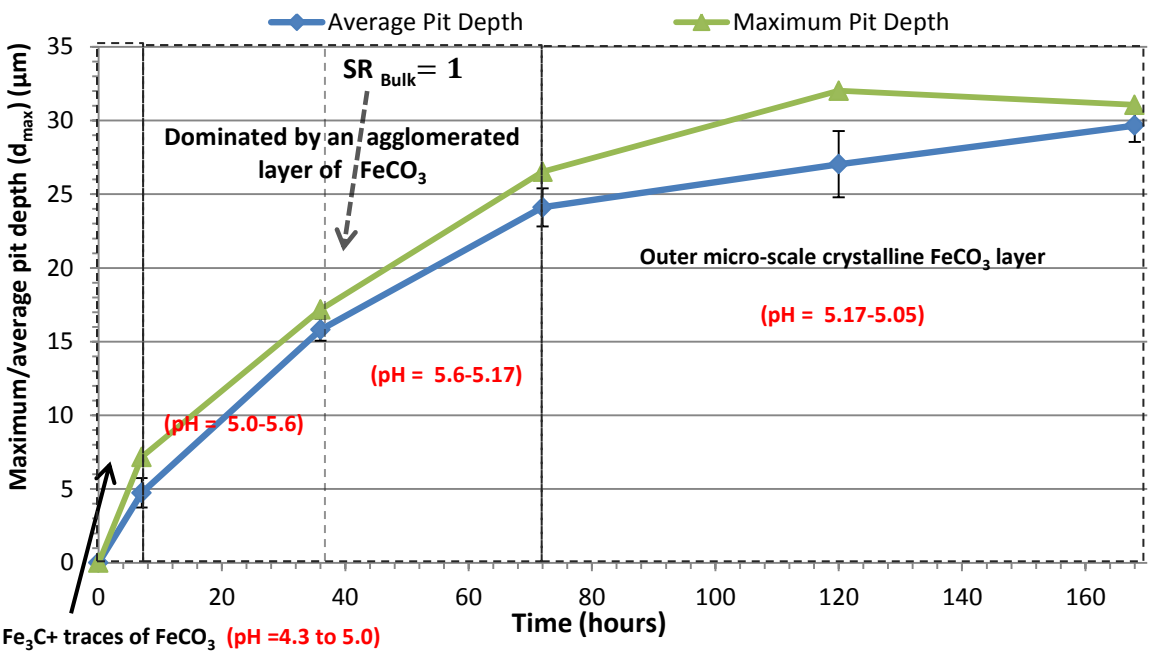

Figure 15: Plot depicting the variation of relative pit depth (maximum and average) with time at 80°C, over a duration of 168 hours in a 10 wt.% NaCl solution saturated with CO_2. Error bars represent the standard deviation based on the 10 deepest pits.

Pitting corrosion damage to carbon steel and pitting factor: It is evident that the pitting corrosion behavior of active steels such as X-65 is significantly different from that of passive materials. Pit growth can usually be easily characterized in passive metals such as stainless steel due to relatively minimal uniform corrosion occurring at surrounding surfaces. On the other hand, significant general corrosion is likely to occur on the surrounding surfaces of an active metal such as carbon steel. This unique scenario results in increased complexity when studying the pit initiation and propagation behavior of carbon steels.

Figure 16 shows the pit depth relative to corroded surface (d_{max}) along with the general thickness loss of the sample surface (P_u) determined from the average LPR corrosion rate as a function of time for all three operating temperatures over each sampling period. A schematic is also provided in Figure 16 for clarity over the values presented.

The results in Figure 16 reflect that at 30°C, the level of depth associated with P_u and d_{max} were relatively similar. However, at temperatures of 50°C and 80°C, the metal penetration as a result of general corrosion (P_u) dominated in comparison to the pit depth relative to the surrounding surface (d_{max}).

In carbon steels, P_u tends to become a much more significant value in comparison to passive materials and should not be neglected when considering the pitting behavior of active materials. Consequently, when assessing pitting rates in such environments, it is perhaps wise to consider the 'absolute pitting rate' (i.e. general thickness loss + pit depth relative to corroded surface, or P_u + d_{max}) as opposed to a 'relative pitting rate' (i.e. pit depth relative to corroded surface, or d_{max}) [11].

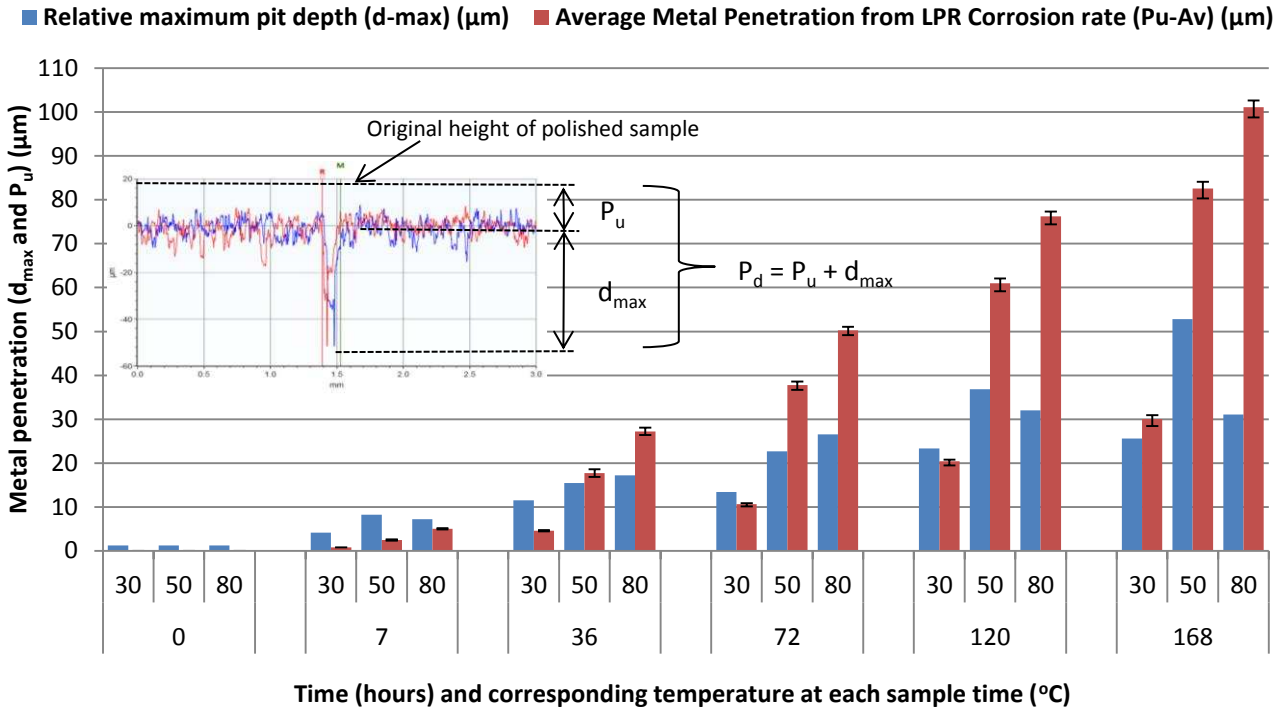

Figure 16: Variation of general material thickness loss and pit depth relative to corroding surface with time for operating temperatures of 30, 50 and 80°C

Figures 17(a) and (b) show the discrepancies observed when analysing the 'absolute' pit depth (P_u + d_{max}) and the 'relative' pit depth (d_{max}). The Figure reflects the importance of understanding the contribution of general corrosion when analysing the propagation of pits. It could be argued that by purely considering the change in pit depth relative to the surrounding corroded surfaces, the actual growth rate of pits are underestimated and effectively masked by high levels of corrosion to the surrounding surface. Such behavior is generally not an issue with respect to passive materials, which exhibit low uniform corrosion rates. The largest discrepancy observed between relative and absolute pit depths occurs predominantly at 50 and 80°C. Despite the marked difference in magnitude, the trend in pit propagation is still the same between each temperature.

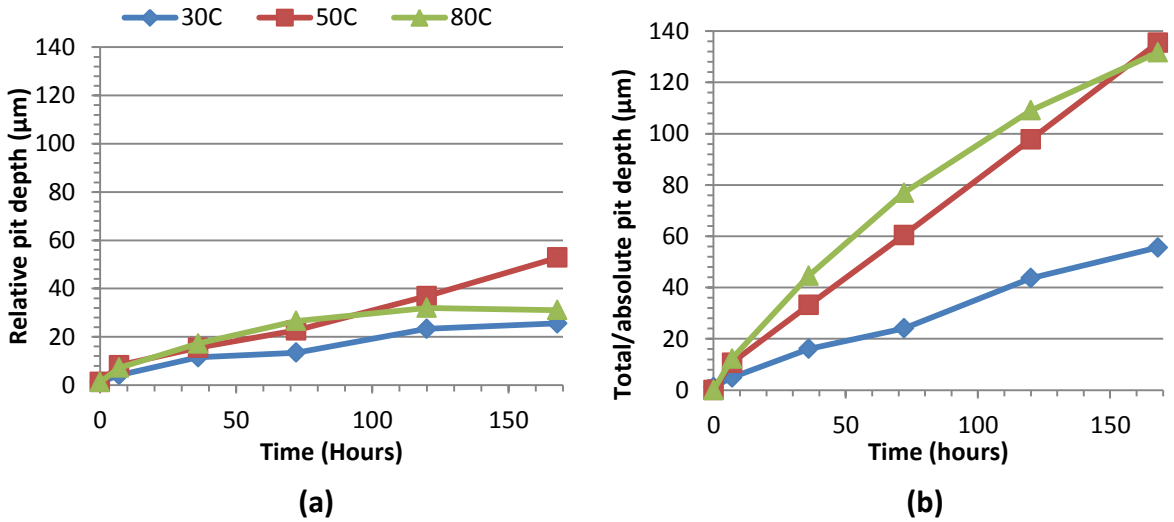

Figure 17: (a) Relative pit depth and (b) total or absolute pit depth vs time for X-65 carbon steel immersed in CO_2 saturated 10 wt.% NaCl solutions at different temperatures over 168 hours of exposure

One method of assessing the extent of pitting corrosion with the system is to perform a pitting factor analysis, referring back to Equation (1). Figure 18 gives a clear indication that the corrosion damage mechanism observed in these conditions is actually pitting even while there is still substantial uniform corrosion taking place in all experiments. Interestingly, towards the end of all three tests, the pitting factors tend towards values between 1.3-1.9. This indicates that over the duration of the tests, the contribution of general corrosion to thickness loss increases as a result of continuous general corrosion along with pitting albeit differently at each temperatures, especially as the buffering effect on *in-situ* pH varies differently with time as shown in Figures 3, 7, 8, 11, 12 and 15. The trend in Figure 18 also indicates a reduction in pitting factor as exposure time increases, before the values stabilize.

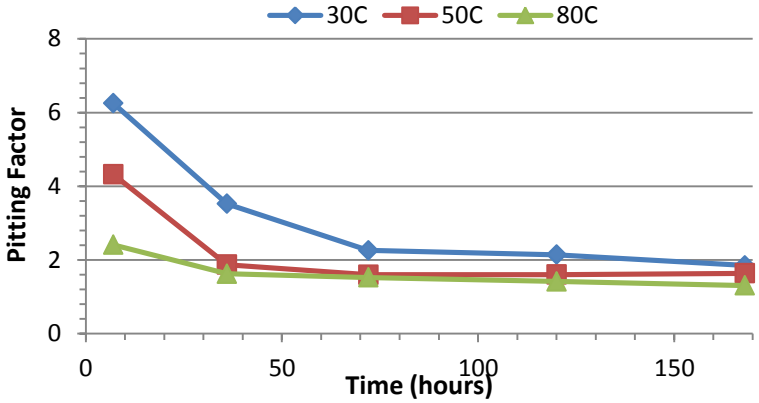

Figure 18: Variation of pitting factor with time for all three test conditions

Absolute pit penetration rate and self-healing mechanism at 80°C: Another method of interpreting pitting behavior within these systems is by analysing the pitting rate. Figure 19 shows the absolute rate of pit growth relative to the surrounding surface, determined from the rate of change in absolute pit depths recorded in Figure 17(b) for each operating temperature. The figure indicates that at 30 and 50°C, the absolute pitting rate appears to stabilize towards the end of the test. However, beyond 72 hours at 80°C, there was a substantial and continuous reduction in the rate of pit growth. This continued reduction coincides with the development of a layer of $FeCO_3$ crystals on top of a layer of initially deposited amorphous/nano-polycrystalline $FeCO_3$.

The relatively slightly higher initial pH (when compared to 30 and 50°C) and hence saturation of the bulk solution is influencing the nucleation and growth of $FeCO_3$ to an extent where crystal sizes are larger than at 50°C. The observed top crystalline layer could be blocking access to some of the active localized sites/pores to aggressive ions from the solution side of corrosion product layer. Such behavior at 80°C has also been reported by Gao et al [23].

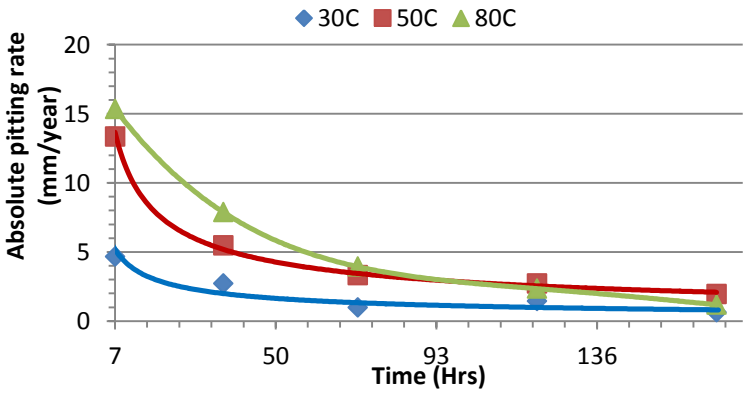

Figure 19: Variation of absolute pit penetration rate with time based on the extent of pit growth over sampling time interval.

To investigate the corrosion product composition underneath the precipitated $FeCO_3$ layer, a cross-section of the corrosion product was removed from the sample surface using a focused ion beam-SEM. This cross-section was subsequently taken to a transmission electron microscope (TEM) for detailed analysis. Figures 20(a) and (b) show that the corrosion product layer formed in the unbuffered corrosion system at 80°C is very porous, with a $FeCO_3$ layer on top and a Fe_3C network between the top layer and the carbon steel substrate. What is most interesting is that traces of $FeCO_3$ were identified within the porous Fe_3C network, and also at the surface of the substrate. It is therefore suggested that a possible self-healing mechanism exists whereby the precipitation of $FeCO_3$ is occurring at the steel surface and within the surface pits, resulting in pit propagation being significantly hindered.

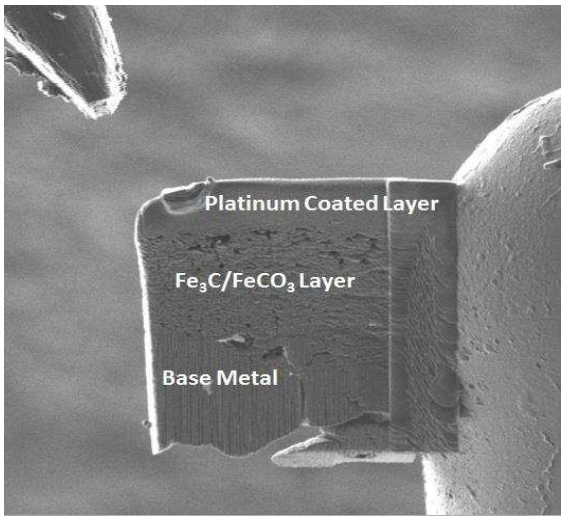

(a)

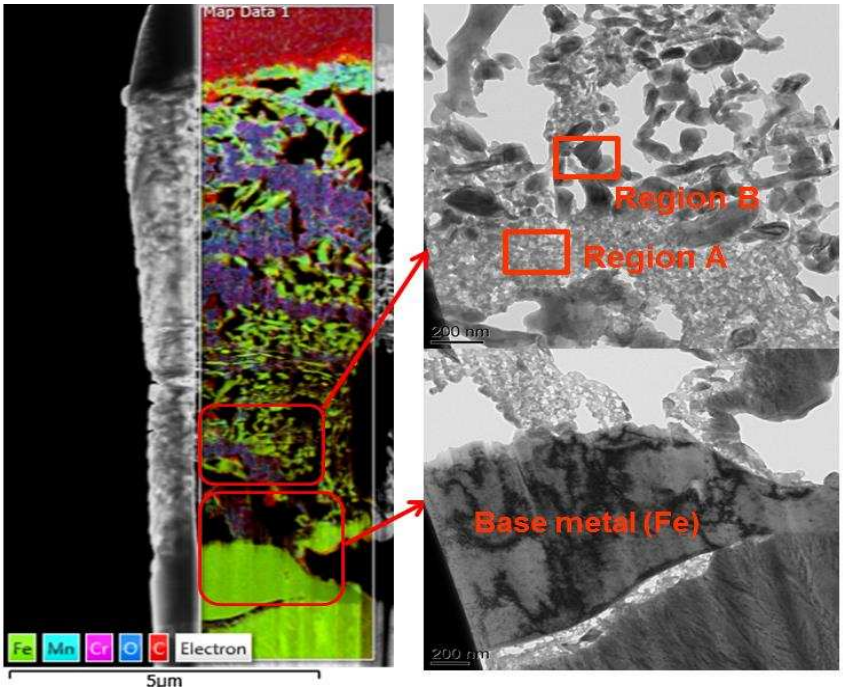

(b)

Figures 20: (a) TEM image of a cross-section of corrosion product on X65 steel exposed to a CO_2 saturated 10 wt. % NaCl at 80°C and after 168 hours. (b) Selected area for EDX mapping and electron diffraction pattern from the TEM.

The presence of $FeCO_3$ was confirmed from elemental analysis using EDX analysis over Regions A and B in Figure 20. The elemental ratios provided in Table 4 indicate the presence of $FeCO_3$ within the Fe_3C network. The suggested self-healing mechanism at 80°C appears to be consistent with observations by Han et al [19]. Such observations have also been attributed to the electro-migration of precipitable anions across a porous corrosion product formed in environments where uniform corrosion precedes corrosion product formation and nucleation of pits [15].

Table 4: Elemental analysis from EDX spectra of regions shown in Figure 20.

Element	Region A Normalized ratio by atm.% relative to carbon	Region B Normalized ratio by atm.% relative to carbon
Fe	1.28	2.99
C	1.0	1.0
O	3.7	0.323
Remarks	Elemental ratio indicative of $FeCO_3$	Elemental ratio indicative of Fe_3C

Further analysis of the corrosion deposits using selected area electron diffraction (provided in Figure 21) produced a continuous ring pattern, confirming that corrosion product is nano-polycrystalline in nature. From the interplanar spacing (d-spacing) of the rings shown in Figure 21, the prescribed indices correspond with $FeCO_3$ [28], confirming that $FeCO_3$ is precipitating underneath the initially formed Fe_3C layer and may well be responsible for the observed reduction in pit growth recorded.

According to Guo et al [22], such a nano-polycrystalline structure of $FeCO_3$ would be expected given the low pH of the system. It is perhaps also worth noting that a typical pH in oilfield environments tends to exist in the range of 4-6 [36]. A schematic representation of the self-healing process of pits at 80°C due to $FeCO_3$ is provided in Figure 22 to aid in summarising the proposed mechanism.

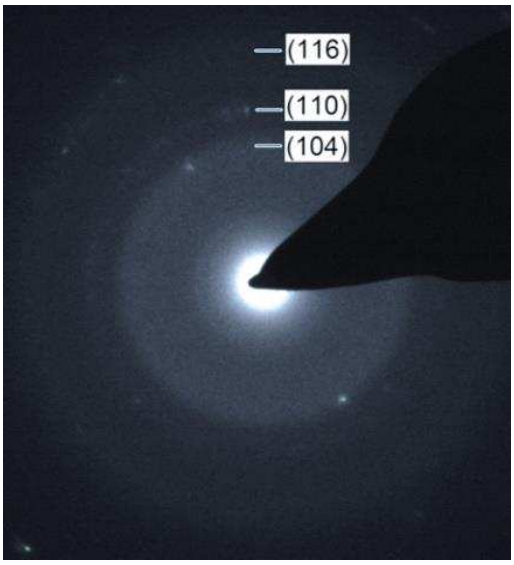

Figure 21: Electron diffraction pattern from TEM analysis of $FeCO_3$ corrosion product underneath initially developed Fe_3C layer on X-65 steel exposed to a CO_2-saturated 10 wt. % NaCl at 80°C for 168 hours.

The schematic of the proposed pit self-healing process occurring at higher temperature is shown in Figure 22 and is considered to be occurring simultaneously with the cumulative effect of continuous uniform corrosion. These are the two combining phenomena that are responsible for lower pit

depth observed in this study but not lower metal penetration. The porous and non-protective nature of corrosion products formed in these conditions could be a very important factor in the manifestation of the pit-self-healing process, especially as it allows for electro-migration of precipitable and/reducible anions such HCO_3^- and/or CO_3^{2-} as suggested by Crolet et al [15]. The implication of this process is the possibility of either of continuous ferrite dissolution to which the walls of the pits are less likely to be shielded from or the build-up of corrosion products within initially active pits. Both of these electrochemical processes remains valid and has been shown to be occurring simultaneously albeit to varying degrees to induce the retardion of pit propagation at 80°C. This observation also asks an important question as to the actual distribution of both anodic and cathodic sites across the depth profile of active pits that has enabled continuous electrochemical activities that could lead to either more localized ferrite dissolution and/or the formation of corrosion products in such confined spaces. If it were to be a passive material such as stainless steel, the localized environment is usually expected to be at a lower pH than the bulk solution at all times and pit propagation will continue unhindered.

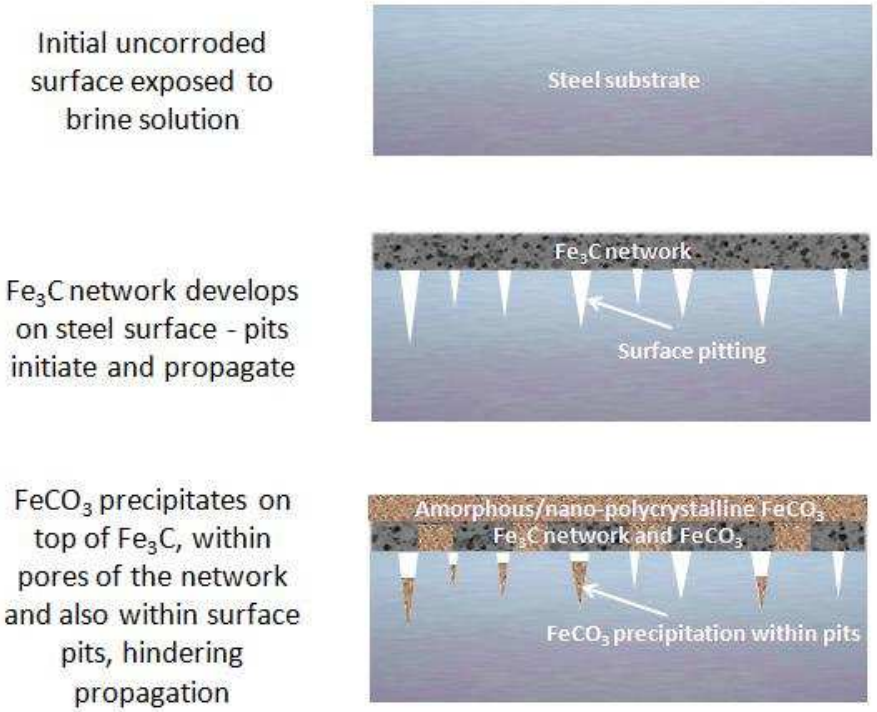

Figure 22: Schematic of the self-healing mechanism of pits proposed for experiments conducted within this publication at 80°C

CONCLUSIONS

A systematic study examining the pitting corrosion behavior of X-65 carbon steel in CO_2-saturated brines has been presented. The paper examines the impact of changes in temperature on the pitting corrosion processes of carbon steel. Pit propagation studies were conducted in static conditions at different operational temperatures. The evolution of surface corrosion product is followed over 168 hours of immersion and their characteristics were related to initiation and growth of pits on the steel surface. The main conclusions which can be drawn from this study are:

- ‘Absolute’ pit depth and ‘absolute’ pit penetration rates are more appropriate terminologies and forms of measurement for the evaluation and characterization of pitting corrosion of carbon steel materials.

- Relative and absolute pitting is strongly related to the morphology of corrosion products deposited on the surface of steel sample.

- The rate of pitting corrosion varies with temperature, especially with respect to the propensity for pits to grow from initiated localized pores.

- Pitting corrosion appears to be the most dominant corrosion mechanism at 50°C, especially when an iron carbide (Fe_3C)/amorphous-like $FeCO_3$ dominates the corrosion products layer.

- Despite general corrosion kinetics being greater at 80^{o}C, the formation of appreciable amounts of nano-polycrystalline $FeCO_3$ on top of an Fe_3C layer and at the steel surface within the pores of the Fe_3C network resulted in a reduction in both uniform and pitting corrosion

- A self-healing mechanism was proposed based on the ability of $FeCO_3$ to precipitate under the Fe_3C network at the steel surface and reduce pit propagation.

- Uniform corrosion kinetics should always be considered in the study of “pitting corrosion” of carbon steel in CO_2-saturated brines and play a vital role in our understanding of the initiation and growth kinetics of pits.

ACKNOWLEDGEMENTS

The authors would like to express sincere appreciation to the Federal Government of Nigeria through the Niger-Delta Development Commission (NDDC) and the University of Leeds for funding this project and providing technical support.

REFERENCES

1. B.D. Craig, *Oilfield metallurgy and corrosion*. 3rd ed. 2004, Denver, Colo.: MetCorr. 282.

2. B.M. Kermani and A. Morshed, "Carbon dioxide corrosion in oil and gas production: A compendium", Corrosion, 59, 08 (2003): p. 659-683.

3. R. Barker, X. Hu, A. Neville, and S. Cushnaghan, "Inhibition of Flow-Induced Corrosion and Erosion-Corrosion for Carbon Steel Pipe Work from an Offshore Oil and Gas Facility", Corrosion, 69, 2 (2012): p. 193-203.

4. R. Barker, X. Hu, A. Neville, and S. Cushnaghan, "Empirical Prediction of Carbon-Steel Degradation Rates on an Offshore Oil and Gas Facility: Predicting CO_2 Erosion-Corrosion Pipeline Failures Before They Occur", Society of Petroleum Engineers Journal, (2013).

5. M.B. Kermani and D. Harrop, "The impact of corrosion on oil and gas industry", SPE Production & Operations, 11, 3 (1996): p. 186-190.

6. L. Zhang, W. Zhong, J. Yang, T. Gu, X. Xiao, and M. Lu. "Effects of temperature and partial pressure on H_2S-CO_2 corrosion of pipeline steel in sour conditions", CORROSION, paper no. 79, (Houston, TX :NACE International, 2011).

7. A. Hernández-Espejel, M.A. Domínguez-Crespo, R. Cabrera-Sierra, C. Rodríguez-Meneses, and E.M. Arce-Estrada, "Investigations of corrosion films formed on API-X52 pipeline steel in acid sour media", Corrosion Science, 52, 7 (2010): p. 2258-2267.

8. Z. Zhu, N. Tajallipour, P.J. Teevens, H. Xue, and F.Y.F. Cheng. "A mechanistic model for predicting localized-pitting corrosion in a brine water-CO_2 system", CORROSION, paper no. 256, (Houston, TX:NACE International, 2011).

9. D.J.D. Garber, D.K. Knierim, M.J. Acuna, and M.K.C. Deokar. "Modelling pitting corrosion in a CO_2 system containing bacteria", CORROSION, paper no. 545, (New Orleans, LA: NACE International, 2008).

10. G. Schmitt and S. Feinen. "Effect of anions and cations on the pit initiation in CO_2 corrosion of iron and steel", CORROSION, paper no.01, (Orlando, FL: NACE International, 2000).

11. R.E. Melchers, "Pitting corrosion of mild steel in marine immersion environment—Part 1; Maximum pit depth", Corrosion, 60, 9 (2004): p. 824-836.

12. S. Papavinasam, A. Doiron, and R.W. Revie, "Model to predict internal pitting corrosion of oil and gas pipelines", Corrosion, 66, 3 (2010): p. 11.

13. A.S.M. International, *Metals Handbook, Ninth Edition: Volume 13-Corrosion (ASM Handbook)*, 1987, ASM International Ohio.

14. J.C. Scully, *The fundamentals of corrosion*. 3rd ed. 1990, Oxford: Pergamon. 250 p.

15. J.L. Crolet, N. Thevenot, and S. Nesic, "Role of Conductive Corrosion Products in the Protectiveness of Corrosion Layers", Corrosion, 54, 3 (1998): p. 194-203.

16. D.R. Lide, *CRC Handbook of Chemistry and Physics: A Ready-reference Book of Chemical and Physical Data*. 2004: CRC Press.

17. A.S.T.M. International, *ASTM Standard G1-03, Standard practice for preparing, cleaning, and evaluating corrosion Test specimens*, in *Annual Book of ASTM Standards; Vol. 03. 02*2003, ASTM International: West Conshohocken, PA.

18. A.S.T.M. International, *ASTM G46-94 Standard Guide for Examination and Evaluation of Pitting Corrosion*, 2005, ASTM International: West Conshohocken, PA. p. 7.

19. J. Han, B.N. Brown, and S. Nešić, "Investigation of the galvanic mechanism for localized carbon dioxide corrosion propagation using the artificial pit technique", Corrosion, 66, 9 (2010): p. 12.

20. F. Farelas, M. Galicia, B. Brown, S. Nesic, and H. Castaneda, "Evolution of dissolution processes at the interface of carbon steel corroding in a CO_2 environment studied by EIS", Corrosion Science, 52, 2 (2010): p. 509-517.

21. Z. Xia, K.C. Chou, and Z. Szklarska-Smialowska, "Pitting corrosion of carbon steel in CO_2-containing NaCl brine", Corrosion, 45, 8 (1989): p. 636-642.

22. S. Guo, L. Xu, L. Zhang, W. Chang, and M. Lu, "Corrosion of alloy steels containing 2% chromium in CO_2 environments", Corrosion Science, 63, (2012): p. 246-258.

23. M. Gao, X. Pang, and K. Gao, "The growth mechanism of CO_2 corrosion product films", Corrosion Science, 53, 2 (2011): p. 557-568.

24. Y. Hua, R. Barker, and A. Neville, "Understanding the Influence of SO_2 and O_2 on the Corrosion of Carbon Steel in Water-Saturated Supercritical CO_2", Corrosion, 71, 5 (2014): p. 667-683.

25. M.M. Antonijevic, S.C. Alagic, M.B. Petrovic, M.B. Radovanovic, and A.T. Stamenkovic, "The Influence of pH on Electrochemical Behavior of Copper in Presence of Chloride Ions", International Journal of Electrochemical Science, 4, (2009): p. 9.

26. M. Abe, M. Kawachi, and S. Nomura, "X-Ray and Neutron Diffraction Studies in Spinel Fe_2MoO_4", Journal of the Physical Society of Japan, 33, 5 (1972): p. 1296-1302.

27. I.G. Wood, L. Vocadlo, K.S. Knight, D.P. Dobson, W.G. Marshall, and G.D.B. Price, J., "Thermal expansion and crystal structure of cementite, Fe_3C, between 4 and 600 K determined by time-of-flight neutron powder diffraction Note:T=540 K", Journal of Applied Crystallography, 37, (2004): p. 9.

28. K.M. H. Effenberger, and J. Zemann, "Crystal structure refinements of magnesite, calcite, rhodochrosite, siderite, smithonite, and dolomite, with discussion of some aspects of the stereochemistry of calcite type carbonates", Z. Kristallogr, 156, (1981): p. 11.

29. F. Deganello, L.F. Liotta, A. Longo, M.P. Casaletto, and M. Scopelliti, "Cerium effect on the phase structure, phase stability and redox properties of Ce-doped strontium ferrates", Journal of Solid State Chemistry, 179, 11 (2006): p. 3406-3419.

30. B. Lavina, P. Dera, R.T. Downs, W. Yang, S. Sinogeikin, Y. Meng, G. Shen, and D. Schiferl, "Structure of siderite $FeCO_3$ to 56 GPa and hysteresis of its spin-pairing transition", Physical Review B, 82, 6 (2010): p. 064110.

31. S. Nesic, J. Postlethwaite, and S. Olsen, "An electrochemical model for prediction of corrosion of mild steel in aqueous carbon dioxide solutions", Corrosion, 52, 04 (1996): p. 280-294.

32. B. Ingham, M. Ko, N. Laycock, N.M. Kirby, and D.E. Williams, "First stages of siderite crystallisation during CO_2 corrosion of steel evaluated using in situ synchrotron small- and wide-angle X-ray scattering", Faraday Discussions, (2015).

33. D.B. Langille and D.C. O'Shea, "Raman spectroscopy studies of anti-ferromagnetic $FeCO_3$ and related carbonates", Journal of Physics and Chemistry of Solids, 38, 10 (1977): p. 1161-1171.

34. L. Bellot-Gurlet, D. Neff, S. Reguer, J. Monnier, M. Saheb, and P. Dillmann, "Raman studies of corrosion layers formed on archaeological irons in various media", Journal of Nano Research, 8, (2009): p. 147-156.

35. S. Guo, L. Xu, L. Zhang, W. Chang, and M. Lu, "Corrosion of alloy steels containing 2% chromium in CO_2 environments", Corrosion Science, 63, 0 (2012): p. 246-258.

36. A. Dugstad, L. Lunde, and S. Nesic. "Control of internal corrosion in multi-phase oil and gas pipelines", Prevention of pipeline corrosion conference, (Houston, TX, 1994).